

Faithful reconstruction of digital holograms captured by FINCH using a Hamming window function in the Fresnel propagation

Nisan Siegel,^{1,2} Joseph Rosen,^{1,2,3} and Gary Brooker^{1,2,*}

¹Department of Biomedical Engineering, Johns Hopkins University, 9605 Medical Center Drive, Rockville, Maryland 20850 USA

²Microscopy Center, Johns Hopkins University Montgomery County Campus, Rockville, Maryland 20850 USA

³Department of Electrical and Computer Engineering, Ben-Gurion University of the Negev, P.O. Box 653, Beer-Sheva 84105, Israel

*Corresponding author: gbrooker@jhu.edu

Received July 22, 2013; accepted August 26, 2013;

posted September 6, 2013 (Doc. ID 194285); published September 30, 2013

Recent advances in Fresnel incoherent correlation holography (FINCH) increase the signal-to-noise ratio in hologram recording by interference of images from two diffractive lenses with focal lengths close to the image plane. Holograms requiring short reconstruction distances are created that reconstruct poorly with existing Fresnel propagation methods. Here we show a dramatic improvement in reconstructed fluorescent images when a 2D Hamming window function substituted for the disk window typically used to bound the impulse response in the Fresnel propagation. Greatly improved image contrast and quality are shown for simulated and experimentally determined FINCH holograms using a 2D Hamming window without significant loss in lateral or axial resolution. © 2013 Optical Society of America

OCIS codes: (090.1760) Computer holography; (090.1970) Diffractive optics; (090.1995) Digital holography; (090.2880) Holographic interferometry; (100.6890) Three-dimensional image processing; (110.0180) Microscopy.
<http://dx.doi.org/10.1364/OL.38.003922>

In Fresnel incoherent correlation holography (FINCH) [1–3], light emitted from an object point is split into two spherical waves and then caused to overlap and interfere at a detection plane, creating a self-referenced Fresnel hologram that consists of the sum of all the Fresnel patterns from all mutually incoherent point sources in the hologram. The recorded digital hologram is then processed computationally by Fresnel propagation to reconstruct an image of the original object scene. Given the potential to achieve super-resolved images of three-dimensional (3D) objects in few exposures [4], it is critical to ensure that the processing algorithms and recording conditions are optimal. Until recently, most FINCH holograms have had long reconstruction distances due to the relative curvatures of the two spherical waves and the minimum curvatures enabled by the hologram-forming optical element [3–5]. In these earlier FINCH implementations [Fig. 1(a)], one spherical wave had a very long focal length f_{d2} approaching infinity, while the other had a shorter focal length f_{d1} of generally 200 mm or more [3–5]. Meanwhile, the detection device (CCD/CMOS camera) was placed at distance z_h , roughly twice the shorter focal length, resulting in a reconstruction distance magnitude of $z_r = |f_{d1} - z_h|$, of at least 200 mm. Now the use of spherical waves of similar curvatures [6–9] in FINCH improves the signal-to-noise (S/N) ratio. In the newer configuration [see Fig. 1(b)] the reconstruction distance has magnitude $z_r = |(f_{d1} - z_h) \cdot (f_{d2} - z_h) / (f_{d2} - f_{d1})|$, which can easily be 10 mm or less. In fact, it is predicted [6] that there are upper and lower limits to the separation between f_{d1} and f_{d2} , beyond which the hologram quality is degraded; so there is incentive to keep the separation and therefore reconstruction distance as close as possible to the lower limit. In examining FINCH holograms created with closely spaced lens patterns, we observed defects in reconstructed images, including poor

contrast, significant amounts of noise and spurious background signal, as well as contrast reversal. Defects of the same type were found consistently at given reconstruction distances, regardless of the quality of the raw hologram or the conditions under which it was recorded, suggesting that these defects were due to the reconstruction process and not due to experimental factors. In this Letter, we show that changing the apodization function of the hologram reconstruction point-spread function (PSF) from a disk window to a Hamming window [10] faithfully restores the image planes throughout the reconstructed volume with smooth transitions between planes similar to what is seen in a conventional optical system. Evaluation of six different window functions revealed that the Hamming window function is the optimal choice to increase final image quality with minimal effect on resolution.

Fresnel propagation [11] is a process of convolving a recorded pattern $g(x, y)$ (in this case a FINCH hologram)

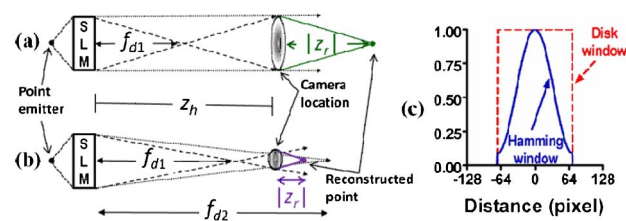


Fig. 1. (a) and (b) Formation and reconstruction of single-point holograms (PSFs) in two FINCH configurations. Objective lenses and other ancillary optics are omitted. (a) Plane and spherical wave and long reconstruction distance. (b) Two spherical waves at the same camera distance but a much smaller recording PSF and shorter reconstruction distance. SLM, spatial light modulator; f_{d1} , signal beam focal length; f_{d2} reference beam focal length; z_h , SLM-detector distance; $|z_r|$, reconstruction distance. (c) Example profiles of disk and Hamming window functions.

with a holographic PSF $h(x, y, z)$ (referred to here as PSF_H) calculated for optical propagation over a defined distance z to produce a reconstructed image $u(x, y, z)$ at distance z . Computationally, it is performed as in Eq. (1):

$$u(x, y, z) = |F_{2D}^{-1}\{F_{2D}[g(x, y)] \times F_{2D}[h(x, y, z)]\}|, \quad (1)$$

where F_{2D} stands for the 2D Fourier transform (FT), F_{2D}^{-1} stands for the 2D inverse FT, and the PSF_H is a Fresnel phase pattern given by

$$h(x, y, z) = \exp\left[\frac{i\pi}{\lambda z}(x^2 + y^2)\right]. \quad (2)$$

In the computation, the hologram and PSF_H are contained in rectilinear arrays with dimensions corresponding to the detector pixel count N_d and must be of matching size. One consideration in using the PSF_H above is the need to ensure that it is always sampled appropriately above the Nyquist limit, since an undersampled Fresnel pattern would give rise to spurious features in the image. It should be noted here that all FINCH optical schemes are designed so that the raw hologram is recorded above the Nyquist sampling rate. For a given wavelength λ , distance z , and pixel size Δ , the minimum number of pixels N_{\min} required to sample the PSF_H above the Nyquist sampling rate is given by Eq. (3):

$$N_{\min} = \lambda z / \Delta^2. \quad (3)$$

It can readily be seen that for common scientific CCD cameras with pixel size $\sim 7 \mu\text{m}$, and at a wavelength of $\sim 550 \text{ nm}$, the PSF_H for distances of hundreds of mm will fill an array equal in size to the detector array used to record the raw hologram without undersampling ($N_d < 2000$ pixels, generally). Thus if the arrays to be convolved are the same size, there is no obvious need to pad or truncate either array to match sizes.

This is not so with PSF_H for much smaller z_r on the order of 10 mm, in which cases the useful information in the PSF_H is limited to a radius of pixels equal to N_{\min} . In such cases, some or most of the PSF_H array is zero-valued once the PSF_H is truncated for a sampling rate below the Nyquist limit. This truncation can be performed by multiplying a disk window function of diameter of $2N_{\min}$ into the PSF_H as an amplitude:

$$h(n_x, n_y, z) = w_d(n_r; N_{\min}) \times \exp\left[\frac{i\pi\Delta^2}{\lambda z}(n_x^2 + n_y^2)\right], \quad (4)$$

where $n_r = \text{round}[\sqrt{n_x^2 + n_y^2}]$, $(n_x, n_y) = (x/\Delta, y/\Delta)$, and

$$w_d(n_r; N_{\min}) = \begin{cases} 1, & n_r \leq \frac{N_{\min}}{2} \\ 0, & \text{otherwise} \end{cases}. \quad (5)$$

Note that $w_d(n_r; N_{\min})$ is dependent on the reconstruction distance z through N_{\min} and Eq. (3). However, use of the disk window leaves a sharp discontinuity in the PSF_H , and the FT of the PSF_H displays undesirable features including high levels of sidelobes. When the reconstructed image is viewed, these spurious PSF_H features induce the negative effects detailed above. These observations are all consistent with the analogous detrimental effects of rectangular

windowing in 1D Fourier analysis in, for example, audio-frequency analysis [12].

To address this problem, it is useful to extend the analogy of audio-frequency analysis: we consider the PSF_H as the recorded signal, which is subject to a window function prior to Fourier analysis. A number of window functions may be used instead of a rectangular function to increase the signal level of the desired frequencies of the recorded function relative to the spurious, undesired frequencies [13]. We examined the following window functions: the exact Hamming, the four-term (-92 dB) Blackman–Harris, Gaussian, the Dolph–Chebyshev, the Tukey (all as described in [13]), and the Planck-taper window [14]. The Hamming window is designed to minimize the first sidelobe in the FT with minimal broadening of the central peak, while the Blackman–Harris is designed to minimize all sidelobes in the FT. The Gaussian and Dolph–Chebyshev windows may be adjusted by changing the exponent and desired sidelobe suppression, respectively, and the Tukey and Planck windows are both piecewise functions of disk windows at the center of the window and tapering functions near the radius of the window, with the proportion of disk to taper controlled by a parameter. We leave the equations for the window functions in the references listed, with the exception of the exact Hamming window $w_H(n_r; N_{\min})$, which we include as an example:

$$w_h(n_r; N_{\min}) = \begin{cases} \alpha - \beta \cos\left[\frac{2\pi(n_r - \frac{N_{\min}}{2})}{N_{\min}}\right], & n_r \leq \frac{N_{\min}}{2} \\ 0, & \text{otherwise} \end{cases}, \quad (6)$$

where $\alpha = 25/46$ and $\beta = 21/46$, values that minimize the first sidelobe in the transform of the window [13]. Both w_d and w_h (and any other window function) are dependent on the reconstruction depth z .

To study the effects of the various PSF_H windows on image resolution, a simulated hologram was used as a model for a point object. An array of 1024×1024 pixels was used, with the input beam into the FINCH system represented as a circularly bounded, uniformly intense plane wave, i.e., all pixels with $n_r < 512$ were given a value of 1. The hologram was calculated modeling the newer FINCH implementation with $z_h = 1.2 \cdot f_{d1} = 0.8 \cdot f_{d2}$, which resulted in a short reconstruction distance, and then reconstructed with all of the PSF_H , and the amplitudes of through-focus reconstruction sequences were used to generate theoretical image point spread functions (PSF_I). The transverse amplitude profiles from each step of a through-focus reconstruction sequence at the index of the peak in the focused image were used as the xz , PSF_I , while transverse profiles were taken from the focused images to give the xy , PSF_I . Representative images of PSF_I and profiles are shown in Fig. 2 for the disk and Hamming windows. In Figs. 2(c) and 2(d), it is shown that the z and xy resolution when using h_h is slightly broadened (by 5% and 8%, respectively), while the nearest sidelobes of the xy profile were reduced 40% in integrated intensity over the neighboring six pixels by the Hamming window function. These factors vary with the other window functions,

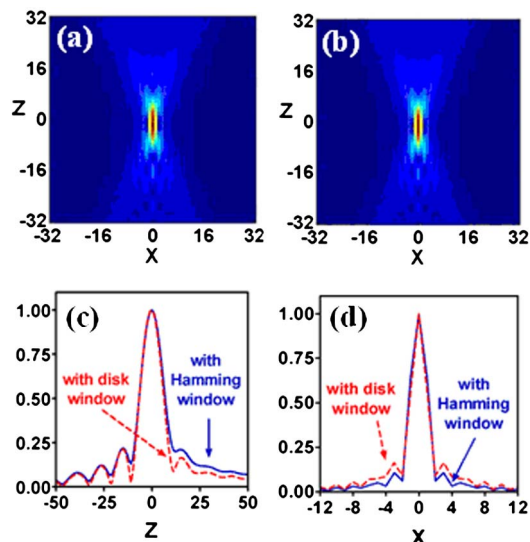


Fig. 2. (a) Calculated xz PSF_I of the reconstructed image of a single point through focus, reconstructed with disk-windowed $PSF_H h_d$. (b) xz PSF_I calculated using the Hamming-windowed $PSF_H h_h$. (c) z -profiles through peak pixel of reconstructions, serving as a measure of relative z resolution. (d) xy profiles of the reconstructions at best focus.

as shown in Table 1 showing the PSF_I widths resulting from various windows, normalized to the PSF_I width resulting from the disk window.

At-focus reconstructed images were also calculated for a set of experimental holograms using the various window functions. All of the images calculated using the nondisk window functions showed some contrast improvement over the one calculated using the disk window, with the exception of the Tukey and Planck windows with taper values of 1 and 0, respectively, which are simply disk windows.

Table 1. Normalized Image Point-Spread Function (PSF_I) Widths for Windowed Holographic Point-Spread Functions (PSF_H)

PSF_H Window	Lateral (xy) PSF_I Width (Normalized)	Axial (xz) PSF_I Width (Normalized)
Disk	1	1
Hamming	1.08	1.05
Gaussian (exponent 2.5)	1.08	1.08
Gaussian (exponent 3.5)	1.23	1.23
Blackman–Harris	1.25	1.25
Dolph–Chebyshev (parameter 3)	1.10	1.06
Dolph–Chebyshev (parameter 4)	1.17	1.14
Tukey (parameter 0)	1.25	1.06
Tukey (parameter 0.1)	1.08	1.06
Tukey (parameter 0.5, 0.9, 1)	1	1
Planck (parameter 0, 0.1)	1	1
Planck (parameter 0.5)	1.02	1.04
Planck (parameter 0.75)	1.17	1.21
Planck (parameter 0.9)	1.27	1.29
Planck (parameter 1)	1.33	1.35

The PSF_I widths here are identical to that of the disk window because, for these parameters, the functions create windows that are exactly or nearly disk windows. The resolution is maintained, but the poor image contrast and quality remain.

A representative sample of these improved images, calculated using the disk and Hamming windows, is shown in Figs. 3(a)–3(d). The improvements due to the Hamming PSF_H window function are quite clear, as the raw hologram was the same in both cases, and the only difference between the two images is the PSF_H that was used. An image reconstructed with the disk-windowed $PSF_H (h_d)$ is noisy enough to partially obscure some features and has an uneven intensity across the image [Figs. 3(a) and 3(c)]. The Hamming-windowed $PSF_H (h_h)$ resulted in significantly reduced noise and spurious background and more even intensity in reconstructed images [Figs. 3(b) and 3(d)]. The improvement by using the Hamming window does not come at significant cost in lateral or axial resolution, as indicated in Fig. 3(e), which shows that the visibility [4] of the smallest features (as a stand-in for modulation transfer function) remains the same (within measurement error) for both disk and Hamming window calculations.

The defects using the disk window vary from image to image within a reconstruction sequence. A further demonstration of this, in a biological sample, is in Fig. 4, showing reconstructed images of pollen grains at three planes. One of the images [Fig. 4(a)] produced with h_d is barely recognizable as a pollen grain, while a second [Fig. 4(b)] is fairly clear, while a third has a significant halo-like background [Fig. 4(c)]; it is difficult to understand what the images show. By comparison, the corresponding images [Figs. 4(d)–4(f)] produced from the same hologram with h_h are all recognizable as images of the pollen at different focus as seen in a standard optical system. Intensity profiles [Figs. 4(g)–4(i)] through three spines of the pollen calculated using the disk (red lines) and Hamming window function (blue lines) quantitatively demonstrate the improved image quality and background suppression at all planes of focus when using the Hamming window. The complete reconstructed series of 100 planes each for h_d and h_h is online.

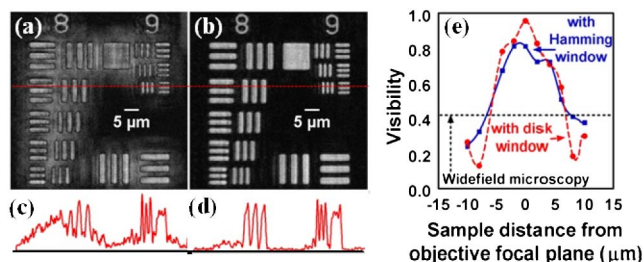


Fig. 3. In (a) and (b), respectively, FINCH reconstructions of the same USAF pattern hologram recorded with dual-lens pattern FINCH (from Fig. 7, top center in [8]), reconstructed with the disk-windowed PSF_H and with the Hamming-windowed PSF_H . Intensity profiles through the lines indicated are shown in (c) and (d). (e) The visibilities of the Group 9 Element 3 bars, as described in [8], from FINCH images of the sample above, at, or below the objective focal plane. The images were reconstructed with either the disk window (red, round points and dashed line) or the Hamming window (blue square points, solid line). The visibility of these features in ordinary wide-field fluorescence microscopy is provided to show that the super-resolving characteristics of FINCH are maintained when using the Hamming window function.

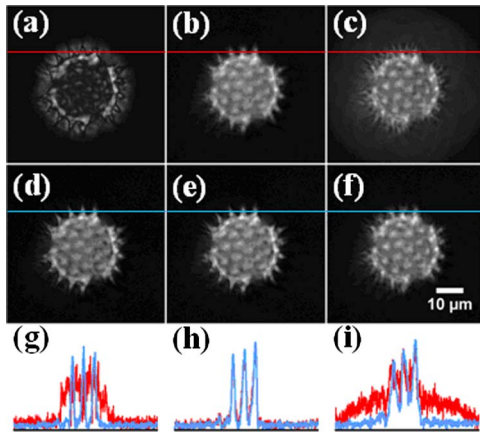


Fig. 4. Reconstructed images of pollen grains from holograms captured with short reconstruction distance. (a)–(c) With disk-windowed PSF_H . (d)–(f) or Hamming-windowed PSF_H . Images 39 [(a) and (d)], 46 [(b) and (e)], and 67 [(c) and (f)] of 100 reconstructed sections from the same holograms are shown. Full series is online (Media 1, top series Hamming window, bottom series disk window). Intensity profiles through three spines at three planes of focus (g)–(i) for disk window (red) or Hamming window (blue).

To provide a more quantitative comparison of the costs and benefits of applying the various window functions, we measured the contrast in the reconstructed images by averaging the pixel intensities in the square feature of USAF groups 8 and 9 and divided that by the average pixel intensity in the void between groups 8 and 9. These contrast values were then normalized to the contrast value obtained using the disk window and were plotted against the normalized PSF_I widths (listed in Table 1) in Fig. 5. It can be seen that the image contrast increases with the PSF_I width. We identified a group of window functions that increased the lateral PSF_I width by less than 10%, a tolerable resolution loss, and which also increased the contrast by at least a factor of 2, sufficient to greatly improve image contrast and perceived quality as well as eliminate contrast reversal and spurious background. These functions are identified in Fig. 5 quadrants (i), showing that the use of these functions does not adversely affect axial resolution more than lateral. The functions represented in quadrant (i) are the exact Hamming window, the Gaussian window with exponent coefficient 2.5, the Dolph–Chebyshev window with parameter of 3 (sidelobe suppression of 30 dB in power), and the Tukey window with taper values of 0 and 0.1. Functions in quadrant (iii) resulted in better resolution but unacceptably poor contrast, while those in quadrant (ii) resulted in improved contrast but unacceptable loss of resolution. Of the functions in quadrant (i), we chose to use the exact Hamming window as it increases the overall PSF_I widths least of these functions.

The 5%–8% loss in maximum resolution when using the Hamming-windowed PSF_H is acceptable, given that the images are so improved in other aspects. This is consistent with Fig. 3, showing the significant improvement in images reconstructed from the experimental holograms in [8] without significantly decreasing the visibilities of the smallest features. This improvement is also seen in Fig. 4. Our results show that use of a smoothly discontinuous PSF_H is critical in faithfully reconstructing FINCH

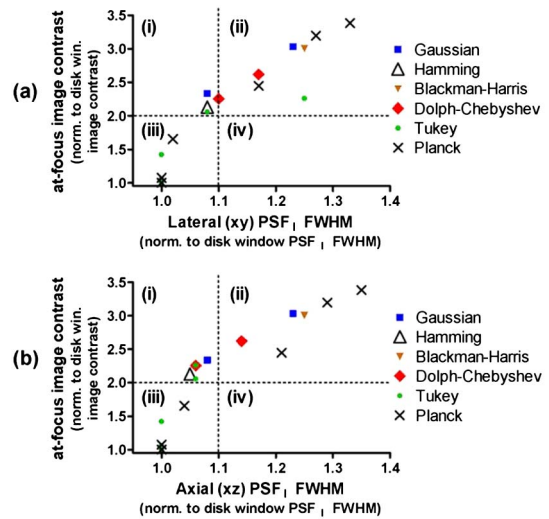


Fig. 5. Contrast in at-focus reconstructed images plotted against PSF_I width of the image. (a) Lateral (xy) PSF_I . (b) Axial (xz) PSF_I . The dashed boxes denote a group of window functions with roughly comparable performance. (a) Window function parameters in quadrant (i): Gaussian, 2.5; Dolph–Chebyshev, 3; Tukey, 0.1; (ii): Gaussian, 3.5; Dolph–Chebyshev, 4; Tukey, 0; Planck, 1, 0.9, and 0.75; (iii): Tukey, 0.5, 0.9, and 1; Planck, 0.5, 0.1, and 0. (b) Window function parameters in quadrant (i): Gaussian, 2.5; Dolph–Chebyshev, 3; Tukey, 0 and 0.1; (ii): Gaussian, 3.5; Dolph–Chebyshev, 4; Planck, 1, 0.9, and 0.75; (iii): Tukey, 0.5, 0.9, and 1; Planck, 0.5, 0.1, and 0.

holograms at short distances and improves the utility of the newly implemented FINCH configurations with small differences between the two spherical waves. Furthermore, the Hamming window function might improve the quality of the reconstructed images from any Fresnel digital hologram, recorded coherently or incoherently.

Supported by NIST Award No. 60NANB10D008, the Israel Ministry of Science and Technology (MOST), the Israel Science Foundation (ISF), and by CellOptic, Inc.

References

- J. Rosen and G. Brooker, *Opt. Lett.* **32**, 912 (2007).
- J. Rosen and G. Brooker, *Nat. Photonics* **2**, 190 (2008).
- G. Brooker, N. Siegel, V. Wang, and J. Rosen, *Opt. Express* **19**, 5047 (2011).
- J. Rosen, N. Siegel, and G. Brooker, *Opt. Express* **19**, 26249 (2011).
- P. Bouchal, J. Kapitan, R. Chmelik, and Z. Bouchal, *Opt. Express* **19**, 15603 (2011).
- B. Katz, J. Rosen, R. Kelner, and G. Brooker, *Opt. Express* **20**, 9109 (2012).
- X. Lai, Y. Zhao, X. Lv, Z. Zhou, and S. Zeng, *Opt. Lett.* **37**, 2445 (2012).
- N. Siegel, J. Rosen, and G. Brooker, *Opt. Express* **20**, 19822 (2012).
- P. Bouchal and Z. Bouchal, *J. Europ. Opt. Soc.* **8**, 13011 (2013).
- R. W. Hamming, *Digital Filters* (Prentice-Hall, 1977), Sec. 5.8.
- J. W. Goodman, *Introduction to Fourier Optics*, 3rd ed. (McGraw-Hill, 2005).
- J. O. Smith, *Spectral Audio Signal Processing* (W3K, 2011).
- F. J. Harris, *Proc. IEEE* **66**, 51 (1978).
- D. J. A. McKechnan, C. Robinson, and B. S. Sathyaprakash, *Class. Quantum Grav.* **27**, 084020 (2010).